Detailed characterization of laboratory magnetized super-critical collisionless shock and of the associated proton energization

W. Yao, A. Fazzini, S. N. Chen, K. Burdonov, P. Antici, J. Béard, S. Bolaños, A. Ciardi, R. Diab, E. D. Filippov, et al.

Detailed characterization of laboratory magnetized super-critical collisionless shock and of the associated proton energization

W. Yao,[1,2,a)] A. Fazzini,[1] S. N. Chen,[3] K. Burdonov,[1,2,4] P. Antici,[5] J. Béard,[6] S. Bolaños,[1] A. Ciardi,[2] R. Diab,[1] E.D. Filippov,[7,4] S. Kisyov,[3] V. Lelasseux,[1] M. Miceli,[8,9] Q. Moreno,[10,11] V. Nastasa,[3] S. Orlando,[9] S. Pikuz,[7,12] D. C. Popescu,[3] G. Revet,[1] X. Ribeyre,[10] E. d'Humières,[10] and J. Fuchs[1]

[1)] *LULI - CNRS, CEA, UPMC Univ Paris 06 : Sorbonne Université, Ecole Polytechnique, Institut Polytechnique de Paris - F-91128 Palaiseau cedex, France*

[2)] *Sorbonne Université, Observatoire de Paris, Université PSL, CNRS, LERMA, F-75005, Paris, France*

[3)] *ELI-NP, "Horia Hulubei" National Institute for Physics and Nuclear Engineering, 30 Reactorului Street, RO-077125, Bucharest-Magurele, Romania*

[4)] *IAP, Russian Academy of Sciences, 603155, Nizhny Novgorod, Russia*

[5)] *INRS-EMT, 1650 boul, Lionel-Boulet, Varennes, QC, J3X 1S2, Canada*

[6)] *LNCMI, UPR 3228, CNRS-UGA-UPS-INSA, Toulouse 31400, France*

[7)] *JIHT, Russian Academy of Sciences, 125412, Moscow, Russia*

[8)] *Università degli Studi di Palermo, Dipartimento di Fisica e Chimica E. Segrè, Piazza del Parlamento 1, 90134 Palermo, Italy*

[9)] *INAF–Osservatorio Astronomico di Palermo, Palermo, Italy*

[10)] *University of Bordeaux, Centre Lasers Intenses et Applications, CNRS, CEA, UMR 5107, F-33405 Talence, France*

[11)] *ELI-Beamlines, Institute of Physics, Czech Academy of Sciences, 5 Kvetna 835, 25241 Dolni Brezany, Czech Republic*

[12)] *NRNU MEPhI, 115409, Moscow, Russia*

(Dated: 27 September 2021)

Collisionless shocks are ubiquitous in the Universe and are held responsible for the production of non-thermal particles and high-energy radiation. In the absence of particle collisions in the system, theoretical works show that the interaction of an expanding plasma with a pre-existing electromagnetic structure (as in our case) is able to induce energy dissipation and allow for shock formation. Shock formation can alternatively take place when two plasmas interact, through microscopic instabilities inducing electromagnetic fields which are able in turn to mediate energy dissipation and shock formation. Using our platform where we couple a fast expanding plasma induced by high-power lasers (JLF/Titan at LLNL and LULI2000) with high-strength magnetic fields, we have investigated the generation of magnetized collisionless shock and the associated particle energization. We have characterized the shock to be collisionless and super-critical. We report here on measurements of the plasma density, temperature, the electromagnetic field structures, and particle energization in the experiments, under various conditions of ambient plasma and B-field. We have also modelled the formation of the shocks using macroscopic hydrodynamic simulations and the associated particle acceleration using kinetic particle-in-cell simulations. As a companion paper of Yao *et al.*[1], here we show additional results of the experiments and simulations, providing more information to reproduce them and demonstrating the robustness of our interpreted proton energization mechanism to be shock surfing acceleration.

I. INTRODUCTION

The acceleration of energetic charged particles by collisionless magnetized shock is a ubiquitous phenomenon in astrophysical environments, among which the most energetic particles are the ultra-high-energy cosmic rays (UHECRs) accelerated in the interstellar medium (ISM)[2,3]. In this case, the source of collisionless dissipation is self-generated electromagnetic fields, resulting from kinetic instabilities such as the Weibel one. Besides, particles are also accelerated in our solar system due to collisionless magnetized shocks developed by the interaction of the solar wind with planetary magnetospheres[4,5] and, at larger distances, with the ISM[6]. In that case, the source of collisionless dissipation is the pre-existing global electromagnetic structure. This will be the case for the experiment detailed here, where we apply a global strong magnetic field onto a laser-ablated fast plasma. Since these shocks usually have their Magnetosonic Mach number $M_{ms} = v_{sh}/v_{ms} \gtrsim 2.7$ (where v_{sh} is the shock velocity, $v_{ms} = \sqrt{C_s^2 + v_A^2}$ is the Magnetosonic velocity, C_s and v_A are the ion sound velocity and Alfvénic velocity, respectively), they belong to the so-called super-critical regime[7,8], which means the shock is not maintained by classical dissipation means alone. In order to help maintain a shock, the additional channel to expel energy is achieved by reflecting particles back upstream[9].

A variety of acceleration mechanisms have been evoked as a way to transfer the energy from the shock waves to the particles, including shock surfing acceleration (SSA),

[a)] Electronic mail: yao.weipeng@polytechnique.edu

shock drift acceleration (SDA), and diffusive shock acceleration (DSA). DSA requires high initial energy before further acceleration[10], thus raising the so-called "injection problem"[11]; while SSA and SDA are believed to be responsible for generating the pre-accelerated seed particles, i.e. for the initial accelerating process from thermal energies. Although it is still under debate whether SSA or SDA dominates the pre-acceleration process in various collisionless shock environments[12–14], we can distinguish them by the following two aspects: On the one hand, in SSA, charged particles first get reflected at the shock front (due to the cross-shock potential electric field), then they surf along the shock front against the convective electric field ($\boldsymbol{E} = -\boldsymbol{v} \times \boldsymbol{B}$), and thus they gain energy. While in SDA, charged particles drift (due to the magnetic field gradient at the shock front) along the convective electric field and then gain energy[15]. On the other hand, SSA requires a thin shock width, compared to the Larmor radius of the charged particles, while SDA needs the opposite (so that the charged particles can gyrate and drift within the shock layer)[10,16].

However, because of the immense spatial scales involved with collisionless phenomenon (e.g. the mean-free-path is $\lambda_{mfp} \sim 1$ AU in the Solar system), only a very small sampling of the shock formation and dissipation mechanisms can be realized. As a result, we still do not have a full understanding of the formation and evolution of collisionless shocks, and the question of the effectiveness and relative importance of SDA and SSA is still largely debated in the literature[17]. To further our understanding, laboratory experiments (and their simulations) have been proven to be an effective tool, providing highly-resolved, reproducible and controllable multi-dimensional datasets that can complement astrophysical observations[18,19]. Below, we will now briefly review the investigation of collisionless shocks via laboratory experiments.

The route that has been up to now most explored in the laboratory is to produce a shock (mediated by the Weibel filamentation instability) by colliding two ablative, unmagnetized flows driven by high-energy nanosecond lasers. This setup has yielded promising results at the Omega Laser Facility[20–22] and the National Ignition Facility (NIF)[23,24], as well as at many other laser facilities all over the world[25–27]. Recently, experiments on collisionless shocks in plasma flows in which there was significant self-generated magnetic field showed, for the first time, the formation of magnetized collisionless shock, with the generation of Weibel instability and observation of electron acceleration in the turbulent structure[28]. Most recently, the dynamics of the ion Weibel instability has been characterized by local, quantitative measurements of ion current filamentation and magnetic field amplification in interpenetrating plasmas via optical Thomson scattering (TS)[29]. What's more, the generation of sub-relativistic shocks, together with relativistic electron acceleration, has been demonstrated to be within the reach of larger-scale, NIF-class laser systems[30].

Another setup relies on a plasma expanding into a preformed ambient magnetized secondary plasma. Thanks to the magnetisation, the target ions create a collisionless magnetic piston that accelerates the ambient plasma to super-Alfvénic velocity, thus creating a high-Mach number shock with velocity of the order of 1000 km/s[31–34]. Recently, Schaeffer et al. have been able to make significant progress in characterizing the formation of collisionless shocks in terms of ion and electron density and temperature, as well as electric and magnetic field strengths as a function of time at OMEGA[35].

Besides, at the LULI laser facility at École Polytechnique (France), collisionless shock waves and ion-acoustic solitons have been investigated by proton radiography[36]. Moreover, significant electron pre-heating via lower-hybrid waves was also achieved in laboratory laser-produced shock experiments with strong magnetic field, providing a potential mechanism for the famous "injection" problem[37]. Additionally, at the VULCAN laser facility at the Rutherford Appleton Laboratory, the temporally and spatially resolved detection of the forming of a collisionless shock was achieved[38].

In contrast to the above schemes, novel setups have been used with ultra-high-intensity lasers. For example, at the XingGuang III laser facility at the Laser Fusion Research Center in China, using a short (2 ps) intense (10^{17} W/cm^2) laser pulse, an electrostatic (ES) collisionless shock, together with the filaments induced by ion-ion acoustic instability, could be observed via proton radiography[39].

In our experimental campaigns at JLF/Titan and LULI2000[1], we investigated shock formation combining laser-produced plasmas, a background medium and a strong ambient magnetic field (as detailed below). We chose to have an expanding plasma to drive a shock into an ambient gas in the presence of a strong external magnetic field. Contrary to Schaeffer *et al.*[33], in our setup, the expanding plasma and the magnetic field were decoupled as the higher Z piston evacuates the magnetic field and was thus unmagnetized. This also allowed us to simultaneously have a highly magnetized ambient plasma (with homogeneous and steady magnetic field) and a high-β piston (as can be seen in Table I, the plasma thermal β of the piston is $\beta \equiv P_{thermal}/P_{mag} \sim 14.0$). Moreover, since our magnetic field strength was more than two times higher[40], reaching 20 T comparing to the 8 T in Schaeffer *et al.*[33], we were able to decouple more strongly the electrons from the ions[41], and the shock was able to fully separate from the piston, which is crucial for its characterization[42]. As a result, we have been able to characterize the plasma density, temperature, as well as the E-field developed at the shock front, and more importantly, observe strong non-thermal accelerated proton populations for the first time.

In this paper, we will first show that laboratory experiments can be performed to generate and characterize globally mildly super-critical, quasi-perpendicular magnetized collisionless shocks in Section II, and detail their

characteristics. Then, we will detail in Section III three-dimensional (3D) magneto-hydrodynamic (MHD) simulations reproducing the laser-driven piston generation and the following shock formation process. In Section IV, with the parameters characterized in the experiment, we will report the results of kinetic particle-in-cell (PIC) simulations, which pinpoint that shock surfing acceleration (SSA) can be effective in energizing protons from the background plasma to hundred keV-level energies.

II. EXPERIMENTAL SETUP AND RESULTS

A. Experimental setup

The experiments were performed at the JLF/Titan (LLNL, USA) and LULI2000 (France) laser facilities with similar laser conditions but using complementary diagnostics, which was mostly linked with the availability of different auxiliary laser beams at each facility.

In the experiment at JLF/Titan, as is shown in Fig. 1 (a–c), the collisionless shock was generated by sending a plasma, generated by having a high-power laser (1 μm wavelength, 1 ns duration, 70 J energy, and 1.6×10^{13} W/cm^2 on-target intensity) irradiating a solid target (Teflon, CF_2), into a low-density (10^{18} cm^{-3}) H_2 ambient gas pulsed from a nozzle prior to the shot, and in the presence of a 20 T magnetic field that is homogeneous and steady-state at the time scale of the experiment. As shown in Fig. 1 (b) and (c), the magnetic field created by a Helmholtz coil system[40,43] was oriented along the y- or z-axis.

In the following experimental campaign at LULI2000, we set up a similar system, shown in Fig. 1 (d). The laser parameters, the ambient H_2 pressure, and the magnetic field strength were the same as in our previous experiment on Titan and detailed above. In this case, due to geometrical constraints, the CF_2 target was tilted by 60° around the z-axis and by 45° around the y-axis, in order to allow the main laser to reach it, as well as to leave access to the Thomson scattering probe beam and collection path.

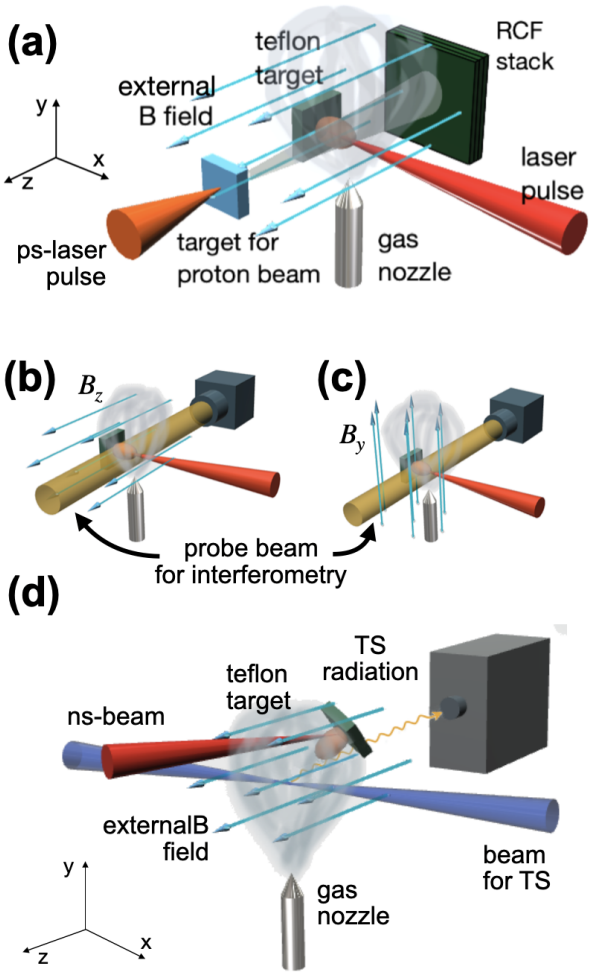

FIG. 1. **Experimental setup and diagnostics used to characterize a magnetized shock.** Proton radiography and interferometry diagnostics have been used alternatively along the axis perpendicular to the laser and to the plasma flow (i.e. the z-axis). (a) Proton radiography setup. (b-c) In the case of interferometry, we could rotate the coil in order to have two different magnetic field orientations with respect to the field of view of the probe beam. (d) Setup of the Thomson scattering (TS) diagnostic fielded at LULI2000.

B. Density characterization through optical interferometry

Using an interferometry setup[44], the plasma electron density is recorded by optically probing the plasma (with a mJ, 1 ps auxiliary laser pulse). In Fig. 2, we present the overall electron density recorded in three different cases.

For the case with both ambient gas and B-field shown in Fig. 2 (a) and (b), the laser irradiation induced the expansion of a hot plasma (the piston) that propagates along the x-axis and the collisionless shock is formed as a consequence of the plasma piston propagating in the magnetized ambient gas[33]. We can clearly see both the piston front and the shock front (indicated by the orange and green arrows, respectively), and indeed they are well detached from each other, enabling us to characterize them separately.

A lineout of the plasma density is shown in Fig. 2 (f), where the piston and shock fronts are also well identified by the abrupt density changes. The piston front is steepened by the compression of the magnetic field (see also below). Besides, we can clearly see a "foot" structure ahead of the shock front in the upstream (US) region for the cases with both ambient gas and B-field, indicating the formation of the magnetized shock[47].

In contrast, for the case with only B-field but without ambient gas[45] shown in Fig. 2 (c) and (d), due to the lack of ambient gas, no collisionless shock is formed ahead of the piston. For the case with only ambient gas but without B-field in Fig. 2 (e), no shock is formed as well

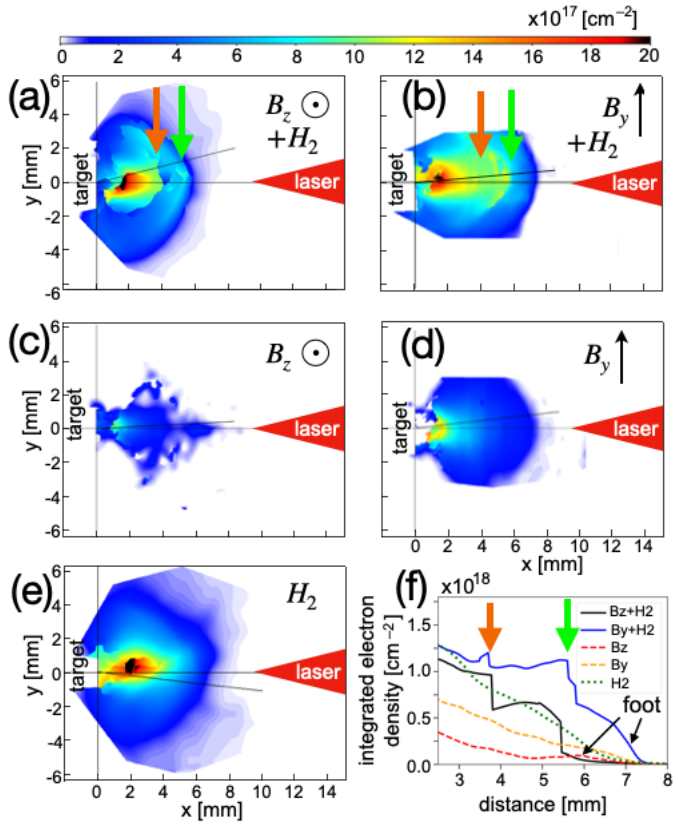

FIG. 2. **Integrated plasma electron density, as measured by optical probing at 4 ns after the laser irradiation of the target, in three different cases.** (a) and (b) Cases with both ambient gas and B-field in the xy- and xz-plane, respectively. (c) and (d) Cases with only B-field but without ambient gas[45,46] in the xy- and xz-plane, respectively. (e) Cases with only ambient gas but without B-field in the xy-plane (the xz-plane will be the same). Each image corresponds to a different laser shot, while the color scale shown at the top applies to all images. The sharp edges on the top and bottom of (b) and (d) are regions blocked by the coil assembly. (f) The lineouts along the thin dark lines shown in each image. The laser comes from the right side and the piston source target is located at the left (at $x = 0$). Yellow arrows indicate the piston front, while green arrows indicate the shock front.

in the ambient gas. From the corresponding lineout in (f), it is clear that only a smooth plasma expansion into the ambient (the green dashed line) can then be seen.

C. Piston compression characterization through X-ray spectroscopy

To further characterize the piston, the x-ray ion emission of Fluorine compressed within the expanding piston was measured by a Focusing Spectrometer with high Spatial Resolution (FSSR)[48] at both laser facilities. It was based on a spherically-bent mica ($2d = 19.9376$ Å) crystal with a curvature radius of $R = 150$ mm. Spatial resolution of 100 μm per pixel was achieved along the plasma expansion. Image Plates (Fujifilm TR BAS) were used as fluorescent detectors. The implemented scheme resulted in 13-16 Å spectral range with a high resolution ($\lambda/d\lambda$ is higher than 1000). It covers spectral lines of Fluorine: resonance H-like (2p–1s transition) and He-like (3p–1s, 4p–1s, 5p–1s etc.) transitions as well as di-electronic satellites to Ly$_\alpha$. The diagnostic allowed us to measure electron density and temperature profiles of the piston expansion using a quasi-stationary approach[49]. The method is based on analysing the relative intensities of spectral lines of the same charge state and also takes into account the recombining plasma with a "frozen" ion charge.

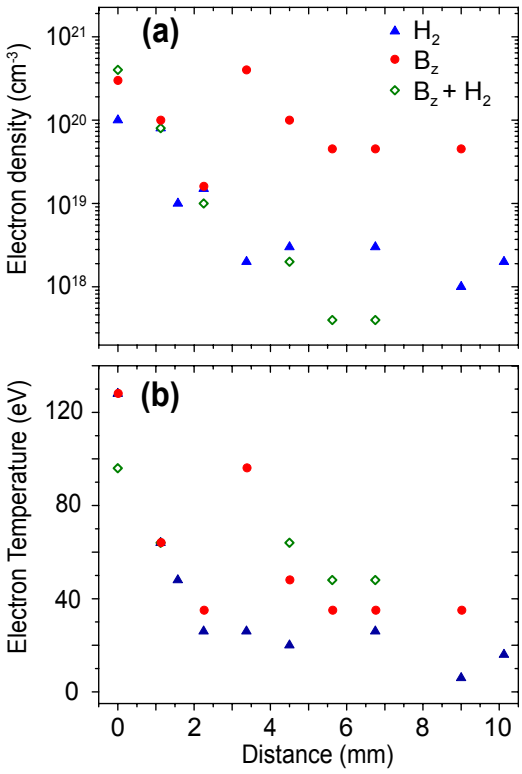

FIG. 3. **FSSR evaluation of (a) electron density and (b) electron temperature of the laser-produced piston in three different configurations (see legend) along the expansion axis.** The measurements are based on the analysis[50] of the relative intensities of the x-ray emission lines of He-like and H-like (see text) Fluorine ions in the expanding plasma in the range of 13-16 Å. The quasi-stationary[49] approach was applied for He-like series of spectral lines assuming a "frozen" ion charge state. The 0 point corresponds to the target surface. A spatial resolution of about 100 μm was achieved. The signal is time-integrated.

Figure 3 (a) shows that obviously the piston encounters stronger hindrance in the case with both ambient gas (H_2) and B-field (B_z) (see the green diamonds), comparing with other cases (i.e. the case with only B_z in red dots and the case with only H_2 in blue triangles). Be-

ing time-integrated, the FSSR deduces an average on-axis volumetric density over the few tens of ns when the plasma density and temperature are high, rather than the time-resolved and line-integrated density measured by optical interferometry. These two diagnostics provide complementary views of the piston. We also see in Fig. 3 (b) that the electron temperature in the case of $B_z + H_2$ becomes the highest at the piston front (between 4 and 7 mm), comparing with other cases. In addition, at the position of 4.5 mm, the evaluated electron density for the case of $B_z + H_2$ is around $2 - 3 \times 10^{18}$ cm^{-3} and the electron temperature is about 65 eV, which are well-reproduced by our FLASH simulations, see Fig. 8 (a) and (b).

D. Electric field characterization through proton radiography

The single shock front was also probed with protons by measuring the local electric field. The probing protons (accelerated by the Target Normal Sheath Acceleration process[51] from an auxiliary target and using the short-pulse arm of Titan) were sent parallel to the B-field, i.e. along the z-axis, as is shown in Fig. 1 (a).

As shown in Fig. 4 (a), we could clearly observe the same structures of the piston front and the shock front, consistent with those observed via optical probe, as shown in Fig. 2.

The synthetic proton radiography shown in Fig. 4 (c) is calculated from a particle tracing code, ILZ[52]. ILZ is a test-particle code using a 3D given distribution of electric and magnetic fields, in order to simulate the trajectories of the protons as they pass through and ballistically propagate afterwards, up to the detector.

As an input for the tracing code we used an electric field E_x with a bipolar spatial profile along the x-axis with a hemispheric geometry in the xz-plane (where z is the axis along which the proton beam propagates) in order to mock up the experimentally observed curvature of the shock front. The same dependence on the coordinates x and z is reproduced along y over a small thickness. The electric field has only a component along x given by:

$$E_x(x,z) = \sqrt{2e}E_0 \frac{x - g(z)}{L} e^{-\frac{(x-g(z))^2}{L^2}} \qquad (1)$$

where E_0 is the maximum field amplitude and L represents the width of the region affected by the electric field. $g(z) = -R/2 + \sqrt{R^2 - z^2}$ represents the shift of E_x along x in order to take into account the hemispherical geometry in the xz-plane and derives directly from the equation of a circumference of radius R centered in $(-R/2, 0)$: $(x + R/2)^2 + z^2 = R^2$. The hemispherical structure has a radius of $R = 5.1$ mm, which is estimated from the experimental proton radiography relative at that time ($t = 5.0$ ns after the laser impact), as is shown in Fig. 4 (a).

We adjust E_0 and L of the ILZ input in order to match the simulated proton dose with the experimental one.

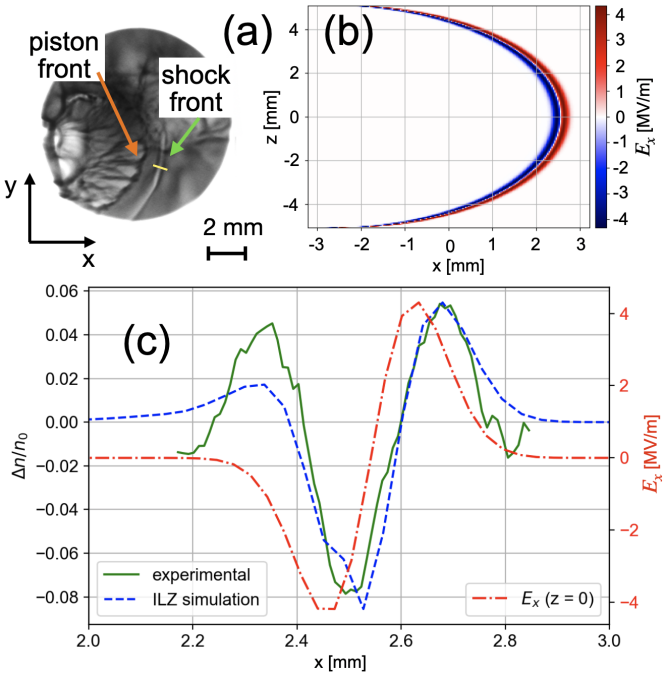

FIG. 4. **Proton radiography** obtained with the setup shown in Fig. 1, 5 ns after the laser pulse. (a) Raw dose collected on the RCF film corresponding to 19 MeV protons. (b) Hemispherical electric field E_x in the xz-plane, with a radius of $R = 5.1$ mm, estimated from (a). (c) Lineout of the proton dose modulation along the yellow line indicated in (a). The green full curve is the modulation from the experimental results, and the dashed blue curve is that from the ILZ simulation, which is obtained by imposing a bipolar electric field with hemispherical shape shown in (b). The red dash-dotted curve represents the lineout of the field E_x in $z = 0$.

The comparison between these two is shown in Fig. 4 (c), where the ILZ simulated modulation was obtained with the field in Eq. 1 with $E_0 = 4.33$ MV/m and $L = 0.12$ mm and shown in Fig. 4 (b).

Note that since the protons are sent along the external magnetic field (i.e. in the z-direction) and since the strength of the magnetic field components in other directions are orders-of-magnitude lower than the externally applied one, the Lorentz force associated with these magnetic field components are much smaller than that induced by the E_x electric field associated with the shock front. As a result, we interpret the proton dose modulation to be caused by electric field only. This assumption is supported by the fact that it yields a simulated proton deflection that is very consistent with the one recorded in the experiment, as can be seen in Fig. 4 (c). Also note that the integration time in a given film is too short to see motion blurring of the moving shock front. Additionally, the amplitude of the electric field at the shock front inferred from the synthetic proton radiography is of the order of MV/m. We will compare it with the particle-in-cell simulation results and discuss them in detail in Sec. IV.

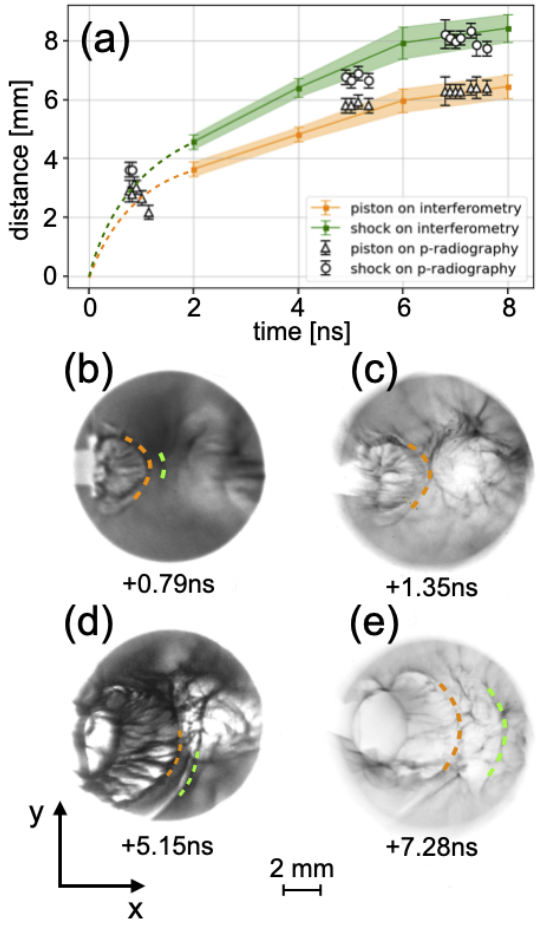

FIG. 5. (a) **Piston and shock front position over time from the electron density (via interferometry) and from the electric field (via proton radiography).** The full green (resp. orange) line materializes the evolution of the shock (resp. piston) location as a function of time as seen on the interferometry diagnostics. It is prolonged toward time 0 by a dashed line passing through the proton radiograph data points at t∼1 ns. (b–e) Images of proton radiography doses at different times, with dashed lines for piston front (in orange) and shock front (in green).

Moreover, we compared the position of the shock structures seen in the electron density (via interferometry) with that in the electric field (via proton radiography) for the case with both external B-field and ambient gas. For the former, we have considered the point where the electron density had a sharp jump, as shown in Fig. 2 (f); as for the latter, we have taken into account the external edges of the proton dose accumulation. As is shown in Fig. 5 (a), the evolution of the piston front and the shock front through both diagnostics are illustrated together (see legends for details), and they clearly show the slowing down of the piston and shock fronts over the first few ns after the laser pulse. Note that when the target was not clearly visible in the radiography, i.e. for the series of points around 5 ns, we made use of the interferometry results to shift all the points of the right amount, while the distances between the piston and the shock fronts were kept constant. The original RCFs for the data points at various times are also shown in Fig. 5 (b-e).

E. Temperature characterization through Thomson scattering

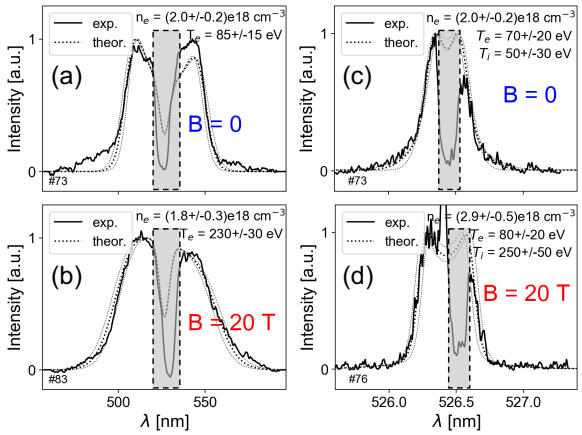

FIG. 6. **Thomson scattering measurements, of the plasma density and temperatures, in the region downstream of the shock front, and for different cases.** (a) measurement on the electron waves for $B = 0$ case (i.e. with only ambient gas), allowing to retrieve the local electron number density and electron temperature, as stated; (b) the same measurement for $B = 20$ T case (i.e. with external B-field and ambient gas). (c) measurement on the ion waves in the plasma for $B = 0$ case, allowing to retrieve the local electron and ion temperatures, as stated; (d) the same measurement for $B = 20$ T case. Solid lines are for experimental data profiles, while dashed lines are for theoretical spectra. The stated uncertainties in the retrieved plasma parameters represent the possible variation of the parameters of the theoretical fit (materialized by the thin dashed grey lines). Note that the deep central dip in the experimental spectra is related to a filter (a black aluminum stripe) which is positioned right before the entrance of the two streak cameras (recording respectively the light scattered off the electron and ion waves). This filter is used to block the very intense and unshifted laser wavelength (the Rayleigh-scattered light), which otherwise would saturate the cameras. Thus, no signal is recorded in this zone, which is materialized by the grey dashed box. The strong narrow peak at around 562.4 nm in panel (d) is caused by leakage of that strong light just at the edge of the filter. The position of the filter can change in the wavelength domain because the diagnostic can be realigned between shots.

With a second high-energy auxiliary laser (526.5 nm wavelength, 1 ns, 15 J) available at LULI2000, we are able to perform Thomson scattering (TS) off the electron and ion waves in the plasma (used in a collective mode[53] and analyzed by different spectrometers). As shown in Fig. 1(d), the collection of the scattered light is performed at 90° (along the z-axis) with respect to the incident di-

rection of the laser probe (the x-axis). The light scattered off the ion (TSi) and electron (TSe) waves in the plasma was analyzed by means of two different spectrometers, set to different dispersions (3.1 mm/nm for TSi and 7.5×10^{-2} mm/nm for TSe), which were coupled to two streak-cameras (Hamamatsu for TSe, and TitanLabs for TSi, both equipped with S-20 photocathode to be sensitive in the visible part of the spectrum, and both with typical 30 ps temporal resolution), allowing us to analyze the evolution of the TS emission in time. The scattering volumes sampled by the instruments were: 120 μm along the x- and y-axes, 40 μm along the z-axis for TSi; 100 μm along the x- and y-axes, 40 μm along the z-axis for TSe. The analysis of the Thomson scattered light was performed by comparison of the experimental images (recorded by the streak cameras) with the theoretical curves of the scattered spectrum for coherent TS in non-collisional plasmas, with the instrumental function width of 5.9 nm for the electron spectrometer and 0.12 nm for the ion spectrometer taken into account. Note that the TS laser probe induces some heating in the hydrogen ambient gas. With the estimate of the electron temperature heated by the TS laser through inverse Bremsstrahlung absorption, we confirm that the upper limit of the TS-induced heating is only around 60 eV, which is significantly smaller than the level of temperatures we observe in the shock[1]. With the above TS diagnostics, we could access spatially and temporally resolved measurements of the plasma density and temperatures (electron and ion) in the upstream (US), as well as in the downstream (DS) region.

Figure 6 shows the TS measurements in the region downstream (DS) compared to the shock front for cases with and without the external B-field. By comparing the experimental data profiles with the theoretical equation of the scattered spectrum for coherent TS in unmagnetized and non-collisional plasmas, with the instrumental function taken into account, we are able to retrieve the local electron number density, as well as the electron and ion temperatures[54]. For the case without the B-field (i.e. with only ambient gas), both TSe and TSi give $n_e \sim 2.0 \times 10^{18}$ cm^{-3} and $T_e \sim 80$ eV, and TSi also gives $T_i \sim 50$ eV in the DS region, as can be seen in Fig. 6 (a) and (c). However, for the case with $B = 20$ T, we see strong heating in the DS region, indicated by the higher temperatures, i.e. $T_e \sim 230$ eV, and $T_i \sim 250$ eV, as can be seen in Fig. 6 (b) and (d).

Note that with a multi-ionic approach (i.e. including C, F and H ions), the theoretical scattering curves are calculated from the distribution functions of each species, weighted by their presence fraction. Due to the natural damping of the other ion species modes, we observe only one mode in the ion acoustic wave (IAW) signal.

With all the above diagnostics, we summarize the characterization of the piston and shock conditions in Table I. Note that for the collisionality, the local magnetic field strength is used. Specifically, the local magnetic field strength of the piston is taken from our FLASH simulation results (in Section III) and that of the shock is from our PIC simulations. While for the calculation of the Mach numbers for the shock, the parameters of the upstream is used.

F. Evidence for proton energization

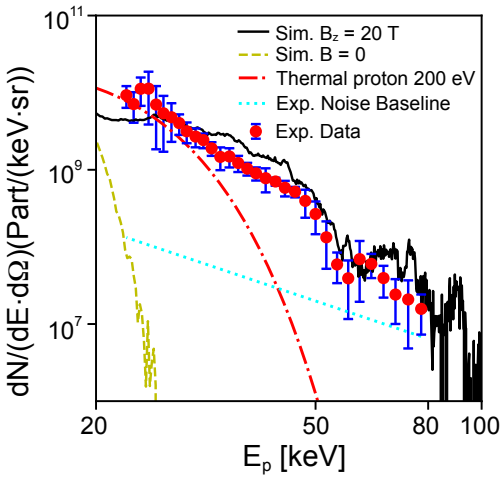

FIG. 7. **Proton energy spectrum.** The experimental data is shown with red dots and blue error bars; the 1D PIC simulation results are shown with black solid line for the case with $B = 20$T and yellow dashed line for $B = 0$ case; the analytical thermal proton spectrum is shown with red dash-dot line (200 eV); and the experimental noise baseline is shown in cyan dotted line. Note that the absolute scale in proton numbers (i.e., the number of protons per bin of energy, divided by the solid angle subtended by the entrance pinhole of the spectrometer) applies only to the experimental spectrum; the simulated spectra are adjusted to the experimental one.

For the observation of the non-thermal proton spectrum, we use a standard magnetic spectrometer, equipped with permanent magnets of 0.5 T strength and a pinhole. It was located close to the target (17.5 cm away) in order to maximize its collection efficiency, and it had its main axis along z, the main axis of the external magnetic field (in an alternate mode to performing TS). Note that having the spectrometer collection axis aligned with that of the magnetic field allows to measure the ions energized out of the plasma[43], which otherwise could not be recorded, as they would be deflected away by the 20 T large-scale magnetic field. We have also used filters in order to eliminate the possibility that the signal observed in the dispersion plane of the spectrometer was originating from heavy ions others than protons from the ambient gas.

That spectrometer has been calibrated precisely with a Hall probe and on many previous campaigns using filters to verify its energy dispersion. The protons are deflected by the magnetic field inside the spectrometer and landed

Region	Piston	Shock
Characterized Plasma Conditions		
Averaged Atomic Number A	17.3	1.0
Effective Charge State Z_{eff}	8.0	1.0
Elec. Number Density n_e [cm^{-3}]	1.0×10^{19}	1.0×10^{18}
Elec. Temperature T_e [eV]	80.0	100.0
Ion Temperature T_i [eV]	40.0	200.0
Flow Velocity V_0 [km/s]	1200.0	1500.0
Local Magnetic Field Strength B [T]	5.0	60.0
Upstream Magnetic Field Strength B [T]	-	20.0
Upstream Elec. Temperature T_e [eV]	-	50.0
Upstream Ion Temperature T_i [eV]	-	20.0
Calculated Parameters		
Ion Collisional mean-free-path ($\lambda_{mfp,i}$) [mm]	6.6×10^{-4}	10.0
Ion Larmor radius ($r_{L,i}$) [mm]	5.4	0.3
Ion Collisionality ($\lambda_{mfp,i}/r_{L,i}$)	1.2×10^{-4}	37.0
Plasma Thermal Beta β_{ther}	14.0	3.4×10^{-2}
Plasma Dynamic Beta β_{dyn}	5.2×10^{3}	2.6
Mach Number M	-	14.0
Alfvénic Mach Number M_A	-	3.4
Magnetosonic Mach Number M_{ms}	-	3.3

TABLE I. **Characterized conditions of piston and shock, as well as the calculated parameters**. $\lambda_{mfp,i} = V_0\tau_i$ is the ion mean-free-path, in which the ion collisional time $\tau_i = 3m_i^{1/2}(kT_i)^{3/2}/(4\pi^{1/2}n_i \ln\Lambda Z^4 q_e^4)$, and $\ln\Lambda \approx 10$ is the Coulomb logarithm, q_e is the elementary charge. $r_{L,i} = m_i V_0/(Zq_eB)$ is the Larmor radius, and the ion collisionality is the ratio of them. The parameters relative to the piston are measured inside the cavity that is located behind the piston front. The thermal (resp. dynamic) beta parameter is the ratio of the plasma thermal (resp. ram) pressure over the magnetic pressure, i.e., $\beta_{ther} = P_{ther}/P_{mag} = 2\mu_0 nkT/B^2$, in which μ_0 is the vacuum permeability, k is the Boltzmann's constant; $\beta_{dyn} = P_{dyn}/P_{mag} = 2\mu_0\rho V_0^2/B^2$, in which $\rho = mn$ is the mass density. For the shock, the Mach number is the ratio of the flow velocity over the sound velocity, $M = V_0/C_s$, in which the sound velocity is $C_s = (\gamma ZkT_e/m_i)^{1/2}$ with $\gamma = 5/3$; the Alfvénic Mach Number is the ratio of the flow velocity over the Alfvénic velocity, $M_A = V_0/V_A$, in which the Alfvénic velocity is $V_A = B/(\mu_0 n_i m_i)^{1/2}$; and the Magnetosonic Mach number is the ratio of the flow velocity over the magnetosonic velocity (see text). For the calculation of the sound velocity and the Alfvénic velocity, we use the parameters of the upstream region.

after a short drift space onto Imaging plates (of TR type), the detector used here. These detectors are absolutely calibrated[55].

The recorded proton spectrum is shown in Fig. 7 with red dots and blue error bars (corresponds to one sigma deviation from the average of 5 shots). Comparing it to the analytical thermal proton spectra (200 eV in red dash-dotted lines, as is observed in[1] through TS), it is clear that the proton energization is non-thermal. The cutoff energy reaches to about 80 keV.

Note that there is no signal recorded above the noise baseline for cases with only the magnetic field or the ambient gas, indicating that the non-thermal particle populations are indeed coming from the shock. We will pinpoint the underlying proton acceleration mechanism with dedicated Particle-in-Cell simulations in Sec. IV.

III. MHD SIMULATIONS WITH FLASH

We use the 3D MHD code FLASH[56] to study the dynamics of the plasma plume expansion and piston formation in the ambient gas with the strong magnetic field, using the same parameters as the JLF/Titan experiment. Note that the piston is collisional and is modeled with a MHD code here; whereas the shock is collisionless and is modeled with a kinetic PIC code in the next section. The simulations are initialized in 3D geometry, using three temperatures (two for the plasma, and one for the radiation) with the equation-of-state of Kemp and Meyer-ter Vehn[57] and radiative transport, in the frame of ideal MHD and including the Biermann battery mechanism of magnetic field self-generation in plasmas[58]. Specifically, the laser beam is normal to a Teflon target foil and has an on-target intensity of 10^{13} W/cm^2; the generated plasma plume expands in the hydrogen gas-jet having an uniform density of 10^{18} cm^{-3}. Moreover, the plasma plume expands in the uniform external magnetic field of 20 T (aligned along the z-axis, as in the experiment).

Figure 8 shows the FLASH simulation results, i.e. the electron density, electron temperature and ion temperature from FLASH at t = 2 ns (after the laser irradiation), in two different cases (the upper row is for the case with only ambient gas but without B-field, while the lower row is for the case with both the ambient gas and the B-field). As FLASH cannot tolerate vacuum, we do not

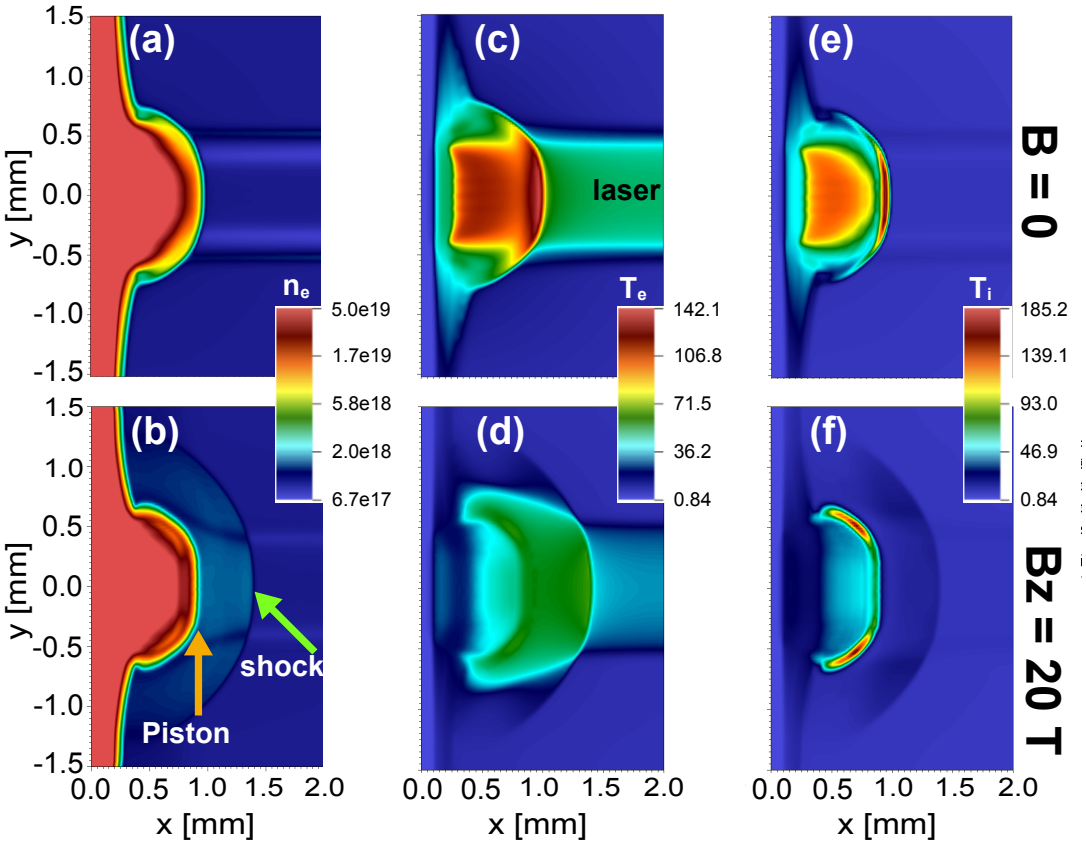

FIG. 8. **FLASH simulation investigating a single shock formation and performed in the conditions of the JLF/Titan experiment.** Maps extracted from FLASH simulations at 2 ns (after the laser irradiation) of: (a) and (b) electron density, n_e in cm^{-3}, (c) and (d) electron temperature, T_e in eV, (e) and (f) ion temperature, T_i in eV. The upper row is for the case without B-field, while the lower row is for the case with B-field. All maps are in linear scale. This XY-plane slice is cut at Z=0. The laser comes from the right side along $y = 0$, and the target is at the left side. The yellow arrow indicates the piston edge, while the green arrow indicates the shock front.

have the FLASH simulation for the case with only B-field but without ambient gas). We can observe that the structures of both the hydrodynamic piston and the induced shock, which propagates inside the ambient, are qualitatively reproduced compared to the experiment, specifically:

The Teflon expanding piston produces a forward shock in the ambient (around $x = 1.4$ mm), as well as a reverse shock inside the Teflon piston (around $x = 0.8$ mm). The electron density is $\sim 1.6\times10^{18}$ cm^{-3} in the forward shock in the gas and increases up to $\sim\ 5\times10^{19}$ cm^{-3} in the reverse shock.

The electron temperatures are between 60 to 70 eV in the forward and reverse shocks. Both correspond quite well to what is measured in the experiment (see the FSSR measurements in Fig. 3 and the TS measurements in[1]). The ion temperature is 15 eV in the forward shock and between 80 eV and 180 eV inside the reverse shock.

Concerning the electron temperature, the FLASH simulation results are two times lower compared to the TS measurements in the DS region shown in Fig. 6; while for the ion temperature, the situation is worse as it is ten times less in the forward shock compared to the TS measurements. Also note that we have not seen the foot structure ahead of the shock in the FLASH simulations.

Such discrepancies between the MHD simulations and the experiments show the difficulties to reproduce the shock condition in our case. This points to the fact that the shock evolution is dominated by kinetic effects. This is why we have resorted to using PIC simulations, the initial conditions of which are taken from the experimental measurements. Nevertheless, we can still observe that the FLASH simulations reproduce well the dynamics of the piston that induces the shock.

Since FLASH has the ability to model magnetic field generation through the Biermann battery effect, it allows us to assess the importance of this effect in the present configuration. Biermann battery generation of magnetic field is typically important only close to the target surface (order of 1 mm), and it is localized over the steep temperature gradients generated by the laser beam and rapidly decays once the laser beam is off (see for example[59–61]). As the shock is induced by the piston in the ambient gas 1 mm away from the target surface after the laser is off

($\sim$ 2 ns), as shown in Fig. 8, the Biermann battery effect is negligible, compared to that of the strong externally applied B-field.

IV. KINETIC SIMULATIONS WITH SMILEI

The proton energization via the collisionless shock is modelled with the kinetic PIC code SMILEI[62]. During the interaction between the shock front and the ambient plasma, as the width of the shock structure ($\sim$mm) is much larger than the thickness of the shock ($\sim \mu$m), we can treat this quasi one-dimensional (1D) interaction, or a thin 1D lineout perpendicular to the curved shock (as shown in Fig. 2) via the 1D3V version of the code.

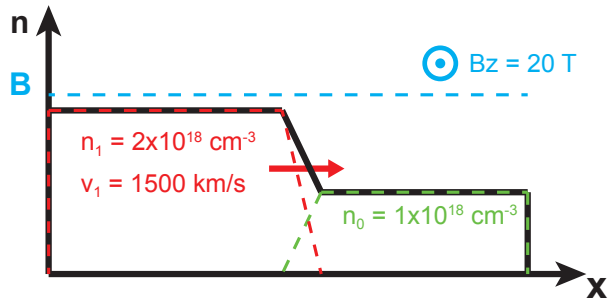

FIG. 9. **Diagram of the PIC simulation setup.** The shocked plasma lies in the left half of the simulation box (red dashed line), drifting towards right; while the ambient plasma lies in the right half (green dashed line). Number density (n), drifting velocity (v), and the magnetic field (B) are noted with their value. We stress here that the shock width is initialized to be equal to the ion inertial length $d_i = 200$ μm.

As is shown in Fig. 9, the ambient plasma lies in the right half of the simulation box, while the left half is for the shocked plasma, flowing towards the right with an initial velocity of $v_1 = 1500$ km/s. Both of them consist of electrons and protons, with the real mass ratio $m_p/m_e = 1836$. The simulation box size is $L_x = 2048 d_e = 11$ mm, and the spatial resolution is $d_x = 0.2 d_e = 1.1$ μm, in which $d_e = c/\omega_{pe} = 5.3$ μm is the electron inertial length, and $\omega_{pe} = (n_{e0} q_e^2/m_e/\epsilon_0)^{1/2} = 5.6 \times 10^{13}$ s^{-1} is the electron plasma frequency. Here, c is the speed of light, $n_{e0} = 1.0 \times 10^{18}$ cm^{-3} is the electron number density of the ambient plasma, and m_e, q_e and ϵ_0 are the electron mass, elementary charge, and the permittivity of free space, respectively. Note that the shock width is initialized to be equal to the ion inertial length $d_i = 200$ μm. The magnetic field is homogeneously applied in the z-direction with $B_z = 20$ T ($\omega_{ce}/\omega_{pe} = 0.06$, where $\omega_{ce} = q_e B/m_e$). The simulation lasts for $1.5 \times 10^5 \omega_{pe}^{-1} \sim 2.5$ ns. Inside each cell, we put 1024 particles for each species. From the perspective of the ion Larmor motion, the simulation size is more than 10 r_{Li}, in which $r_{Li} = v_1/\omega_{ci} = m_i v_1/q_e B \sim 0.8$ mm.

For the shocked plasma, the electron number density is $n_{e1} = 2n_{e0} = 2.0 \times 10^{18}$ cm^{-3}, and the temperature is $T_{e1} = 100$ eV and $T_{i1} = 200$ eV, all inferred from the TS characterization[1]. The boundary conditions for both particles and fields are open, and enough room is left between the boundary and the shock, so that the boundary conditions do not affect the concerned physics. Given the initial low temperature of the ambient plasma in the simulation ($T_{e0} = 50$ eV), the Debye length is small compared to the grid resolution d_x, i.e. $\lambda_{De} = (\epsilon_0 k T_{e0}/n_{e0} q_e^2)^{1/2} \approx 0.01 d_e = 0.05 d_x$. However, we do run a series of simulations with different initial temperatures, showing that the energy conservation for those cases is limited around 0.05% and the physical results are almost the same. The mean-free-path of the presented case is $\lambda_{mfp} \approx 1800 d_e$, which is larger than the interaction scale, further confirming that the shock is collisionless.

We report in Fig. 10 the results of two PIC simulations, i.e. with and without B-fields. For the case with the applied B-field (on the left column), typical structures of a super-critical quasi-perpendicular collisionless shock can be seen[9]. For example, the overshoot in the DS region (on the left of the red dashed line), the ramps in the shock fronts (both the red dashed line and the cyan dotted line), and the foot in the upstream (US) region, as can be seen in Fig. 10 (a). This foot region is formed by the reflected protons at a distance within $r_{L,i}$ and modulated by the modified two-stream instability[63]. The proton density (n_i) in Fig. 10 (e) shows a compression ratio of $n_{i,DS}/n_{i,US} \approx 4$, which agrees with the theoretical jump condition prediction[64]. This density profile, together with the transverse electric field E_y (not shown here), also follows the distribution of the external applied B-field B_z. The longitudinal electric field (E_x) in Fig. 10 (c) peaks right at the ramps, providing the electrostatic cross-shock potential to trap and reflect the protons, as can be seen in the phase-space distribution in Fig. 10 (g). Because the proton reflection is clearly due to E_x in our case, not the DS compressed B-field[10], together with the fact that the ion Larmor radius (about 0.8 mm) is larger than the shock width (around 200 μm), the dominant particle acceleration mechanism is SSA, not SDA. Note that the cyan dotted line indicates one of the periodic shock reformation[9]. On the contrary, for the case without B-field (on the right column), the drifting plasma just penetrates through the ambient gas and no shock is formed, thus no proton energization can take place, which is in accordance with our experimental observation.

We note that the bipolar structure of the E_x electric field at the front displayed in Fig. 10 (c) matches the one that was retrieved from the proton radiography data, as shown in Fig. 4. Such structure seen in the 1D PIC simulations is also verified in the complementary 2D simulations that will be detailed below. Now, we also note that, quantitatively, in Fig. 10 (c), the PIC simulation gives an amplitude of the longitudinal electric field $E_x \sim 5 \times 10^8$ V/m in the shock layer, which is two order-of-magnitude higher than the fitting of the proton radiography in Fig. 4

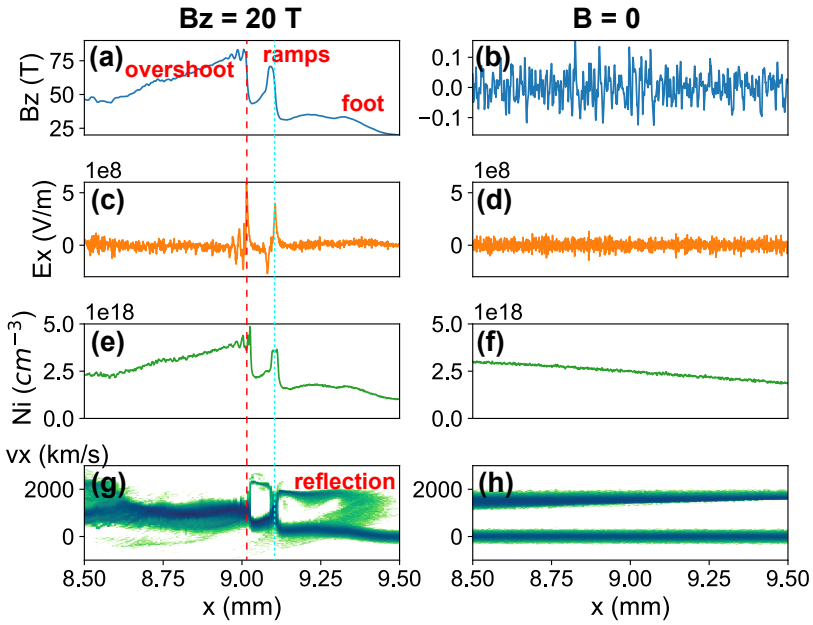

FIG. 10. **Features of the super-critical quasi-perpendicular collisionless shock structure in ion density and EM fields distribution (with and without the external magnetic field), which prove the dominant particle acceleration mechanism to be SSA.** Specifically, (a) and (b) transverse magnetic field B_z; (c) and (d) longitudinal electric field E_x; (e) and (f) ion density profile; (g) and (h) phase-space distribution $x - v_x$ at the end of the simulation, i.e. at $t = 2.7$ ns. The case with B-field is on the left column, while that without is on the right. The red dashed line and the cyan dotted line indicate the position of the shock ramps.

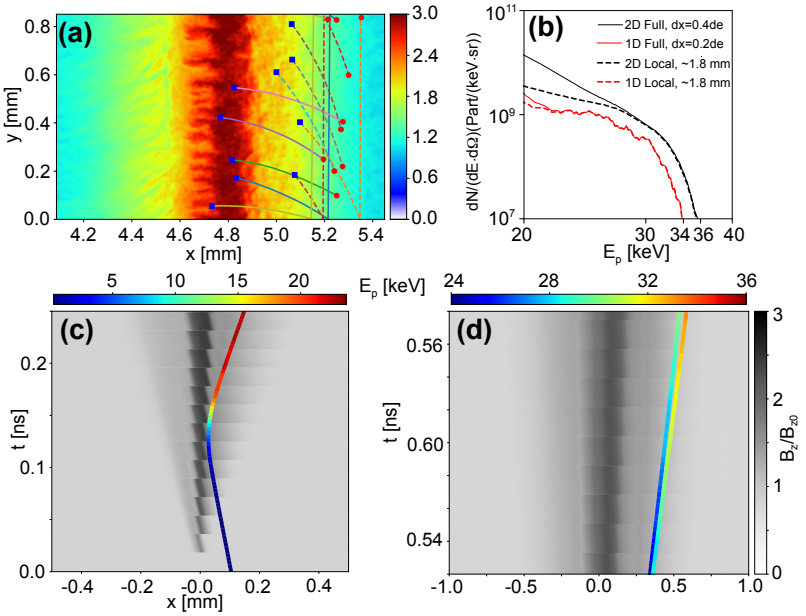

FIG. 11. **2D simulation results.** (a) B-field maps at 0.7 ns, normalized to 20 T, with trajectories of protons ($E_k > 30$ keV). Solid lines are for protons from the ambient plasma and dashed ones are for protons from the drifting plasma; blue squares are the starting position at 0.5 ns, while red dots are the ending position at 0.7 ns. (b) Energy spectra of both 1D and 2D simulation results at 0.7 ns. Red lines are for the 1D case (solid line for protons in the whole simulation box, dashed line for those which lie around the shock layer in the vicinity of 1.8 mm), while black lines are for the corresponding 2D one. (c) Trajectory of a proton reflected at the shock front in the $x - t$ diagram, overlaid on the transversely-averaged B-field map in the reference frame of the contact discontinuity (the grey colorbar is for the B-field strength, while the colored one is for the proton kinetic energy). (d) Trajectories of two protons surfing along the shock front, also in the $x - t$ diagram, overlaid on the transversely-averaged B-field map in the same reference frame.

(c). This discrepancy regarding the amplitude of the field between the simulation and the experiment may be due to several reasons: firstly, the bipolar electric field structure fitted in the proton radiography has a size of 0.4 mm, while the E_x peaks in the PIC simulations are very sharp, with their width smaller than 0.02 mm. With a time-average of the PIC simulation over 0.2 ns, the E_x profile around the shock front reaches a size of 0.4 mm, and its value drops down to 2×10^7 V/m. Secondly, the PIC simulation represents the tip of the semi-sphere shaped expanding shock front at a single slice of z-direction, where the B-field is strictly perpendicular to the plasma flow and the shock is the strongest ((as sketched in Fig. 4 (b))); however, the proton radiography covers the whole shock front with an integration along the z-direction. It includes all other plasma flow directions in the xz-plane, which are not perpendicular to the B-field and the corresponding shocks are weaker. This is what was already considered in the analysis of the proton radiography data, as shown in Fig. 4. Last but not least, the amplitude of the electric field is decreasing with time. In our 1D PIC simulation, the results are at $t = 2.7$ ns (from the shock formation); while in the experimental case, the proton radiography results are at $t = 5.0$ ns (from the laser impact). Hence, we can expect that the early-time PIC field is higher than that derived from radiographs taken at later time.

Particle dynamics of a high-velocity shock (as well as the comparison with the low-velocity case) and of the subsequent shock surfing proton energization is detailed in our previous paper[1], while here we focus on demonstrating the robustness of the SSA mechanism that is at play in our experiment via 2D simulations, taking the non-stationarity[65] into consideration. Due to the limitation of the computational resources, we reduce the 2D simulation scale to an acceptable level: the simulation box sizes are $L_x = 8$ mm, $L_y = 0.8$ mm, the simulation time $t_{end} = 0.7$ ns, and the resolution is $d_x = 0.4d_e$.

From Fig. 11 (a), we can clearly see that the transverse non-stationarity has already occurred, with 2D-stripes mostly positioned at/behind the shock layer; while for protons with kinetic energy above 30 keV, their trajectories show that they mainly appear at the shock front, travelling down the negative y-direction. Note that the convective electric field $\boldsymbol{E} = -\boldsymbol{v} \times \boldsymbol{B}$ is towards the positive y-direction, i.e. $E_y = v_x B_z$; and the drifting of the protons against the convective electric field serves as a distinctive feature that the dominating proton acceleration mechanism is SSA, not SDA[15]. Fig. 11 (b) shows the proton energy spectra at 0.7 ns of both the 1D and 2D cases, which are close to each other, and there is only a 2 keV difference in the highest energy cut, which can be caused by the numerical heating of the 2D case (with lower spatial resolution). Moreover, checking the energy evolution of the protons in the $x - t$ diagram, overlaid on the transversely-averaged B-field map in the reference frame of the contact discontinuity (CD), it is clearly demonstrated that the accelerated proton is first reflected at (or, picked up by) the shock front in Fig. 11 (c), and then surfing along the shock front while keeping gaining energy in Fig. 11 (d). This is exactly the same picture as we have shown for the 1D simulations[1], proving that the SSA is the dominating proton acceleration mechanism at play (even in the multi-dimensional case).

Nevertheless, the non-stationarity of the shock might further accelerate the proton at a later time, especially after the protons pass through the shock front and gyrate in the DS region. But unfortunately right now we do not have the computational resources to reveal that scenario. In short, our 2D simulation shows that the non-stationarity does not prevent the protons from being accelerated by SSA (reflecting and surfing), at least not at an early time.

V. CONCLUSIONS

In conclusion, we have shown that laboratory experiments can be performed to generate and characterize globally mildly super-critical, quasi-perpendicular magnetized collisionless shocks. More importantly, non-thermal proton spectra are observed for the first time, and the underlying acceleration mechanism is pinpointed to be SSA via kinetic simulations, which can remarkably reproduce the experimental proton spectra. Such laboratory studies for proton acceleration, as well as those for electrons reviewed above, can not only further our understanding of the shock formation and evolution by complementing spacecraft and remote sensing observations, but also help shed new light on solving the fundamental issue of injection for the UHECR production.

Our platform can be tuned in the future to perform a systematical study of collisionless shocks with different B-field strength and orientation, enabling us to capture the transition of magnetized collisionless shocks from the sub-critical regime to the super-critical one, so that we can explore the triggering of the other acceleration scenarios (e.g. SDA and DSA).

ACKNOWLEDGMENTS

The authors would like to thank the teams of the LULI (France) and JLF laser (USA) facilities for their expert support, as well the Dresden High Magnetic Field Laboratory at Helmholtz-Zentrum Dresden-Rossendorf for the development of the pulsed power generator used at LULI. We thank the Smilei dev-team for technical support; we thank P. Loiseau (CEA-France) for the Thomson scattering analysis code as well as R. Riquier (CEA-France) for the ILZ code. We also thank Ph. Savoini (Sorbonne U., France), L. Gremillet, C. Ruyer (CEA-France), and M. Manuel (General Atomics, USA), and Ph. Korneev (MEPHI, Russia) for discussions. W.Y. would like to thank R. Li (SZTU, China) for discussions. This work was supported by funding from the European

Research Council (ERC) under the European Unions Horizon 2020 research and innovation program (Grant Agreement No. 787539). The computational resources of this work were supported by the National Sciences and Engineering Research Council of Canada (NSERC) and Compute Canada (Job: pve-323-ac). Part of the experimental system is covered by a patent (1000183285, 2013, INPI-France). The FLASH software used was developed, in part, by the DOE NNSA ASC- and the DOE Office of Science ASCR-supported Flash Center for Computational Science at the University of Chicago. We thank J. L. Dubois for providing us EOS and opacities. The research leading to these results is supported by Extreme Light Infrastructure Nuclear Physics (ELI- NP) Phase II, a project co-financed by the Romanian Government and European Union through the European Regional Development Fund, and by the project $ELI-RO-2020-23$ funded by IFA (Romania). JIHT RAS team members are supported by the Ministry of Science and Higher Education of the Russian Federation (State Assignment No. 075-00460-21-00). The reported study was funded by the Russian Foundation for Basic Research, project No. 19-32-60008.

[1]W. Yao, A. Fazzini, S. Chen, K. Burdonov, P. Antici, J. Béard, S. Bolaños, A. Ciardi, R. Diab, E. Filippov, *et al.*, *Laboratory evidence for proton energization by collisionless shock surfing*, Nature Physics (2021).

[2]E. A. Helder, J. Vink, C. G. Bassa, A. Bamba, J. A. M. Bleeker, S. Funk, P. Ghavamian, K. J. van der Heyden, F. Verbunt, and R. Yamazaki, *Measuring the Cosmic-Ray Acceleration Efficiency of a Supernova Remnant*, Science **325**, 719 (2009).

[3]S. Nikolić, G. van de Ven, K. Heng, D. Kupko, B. Husemann, J. C. Raymond, J. P. Hughes, and J. Falcón-Barroso, *An Integral View of Fast Shocks Around Supernova 1006*, Science **340**, 45–48 (2013).

[4]D. L. Turner, T. Z. Wilson III, L. B. Liu, I. J. Cohen, S. J. Schwartz, A. Osmane, J. F. Fennell, J. H. Clemmons, J. B. Blake, J. Westlake, B. H. Mauk, A. N. Jaynes, T. Leonard, D. N. Baker, R. J. Strangeway, C. T. Russell, D. J. Gershman, L. Avanov, B. L. Giles, R. B. Torbert, J. Broll, R. G. Gomez, F. S. A., and J. L. Burch, *Autogenous and efficient acceleration of energetic ions upstream of earth's bow shock*, Nature **561**, 206–210 (2018).

[5]T. Amano, T. Katou, N. Kitamura, M. Oka, Y. Matsumoto, M. Hoshino, Y. Saito, S. Yokota, B. Giles, W. Paterson, *et al.*, *Observational evidence for stochastic shock drift acceleration of electrons at the earth's bow shock*, Physical Review Letters **124**, 065101 (2020).

[6]R. Decker, S. Krimigis, E. Roelof, M. Hill, T. Armstrong, G. Gloeckler, D. Hamilton, and L. Lanzerotti, *Mediation of the solar wind termination shock by non-thermal ions*, Nature **454**, 67–70 (2008).

[7]F. Coroniti, *Dissipation discontinuities in hydromagnetic shock waves*, Journal of Plasma Physics **4**, 265–282 (1970).

[8]J. Edmiston and C. Kennel, *A parametric survey of the first critical mach number for a fast mhd shock*, Journal of Plasma Physics **32**, 429–441 (1984).

[9]A. Balogh and R. A. Treumann, *Physics of collisionless shocks: space plasma shock waves* (Springer New York, New York, NY, 2013).

[10]G. Zank, H. Pauls, I. Cairns, and G. Webb, *Interstellar pickup ions and quasi-perpendicular shocks: Implications for the termination shock and interplanetary shocks*, Journal of Geophysical Research: Space Physics **101**, 457–477 (1996).

[11]B. Lembège, J. Giacalone, M. Scholer, T. Hada, M. Hoshino, V. Krasnoselskikh, H. Kucharek, P. Savoini, and T. Terasawa, *Selected problems in collisionless-shock physics*, Space Science Reviews **110**, 161–226 (2004).

[12]R. Burrows, G. Zank, G. Webb, L. Burlaga, and N. Ness, *Pickup ion dynamics at the heliospheric termination shock observed by voyager 2*, The Astrophysical Journal **715**, 1109 (2010).

[13]G. Zank, J. Heerikhuisen, N. Pogorelov, R. Burrows, and D. McComas, *Microstructure of the heliospheric termination shock: Implications for energetic neutral atom observations*, The Astrophysical Journal **708**, 1092 (2009).

[14]S. Chalov, Y. Malama, D. Alexashov, and V. Izmodenov, *Acceleration of interstellar pickup protons at the heliospheric termination shock: Voyager 1/2 energetic proton fluxes in the inner heliosheath*, Monthly Notices of the Royal Astronomical Society **455**, 431–437 (2016).

[15]F. Guo and J. Giacalone, *The acceleration of thermal protons at parallel collisionless shocks: three-dimensional hybrid simulations*, The Astrophysical Journal **773**, 158 (2013).

[16]Z. Yang, Q. Lu, B. Lembège, and S. Wang, *Shock front nonstationarity and ion acceleration in supercritical perpendicular shocks*, Journal of Geophysical Research: Space Physics **114** (2009).

[17]Z. Yang, B. Lembège, and Q. Lu, *Impact of the rippling of a perpendicular shock front on ion dynamics*, Journal of Geophysical Research: Space Physics **117** (2012).

[18]R. Paul Drake, *High Energy Density Physics: Fundamentals, Inertial Fusion and Experimental Astrophysics* (Springer-Verlag Berlin Heidelberg, 2006).

[19]S. Lebedev, A. Frank, and D. Ryutov, *Exploring astrophysics-relevant magnetohydrodynamics with pulsed-power laboratory facilities*, Reviews of Modern Physics **91**, 025002 (2019).

[20]W. Fox, G. Fiksel, A. Bhattacharjee, P.-Y. Chang, K. Germaschewski, S. Hu, and P. Nilson, *Filamentation instability of counterstreaming laser-driven plasmas*, Physical Review Letters **111**, 225002 (2013).

[21]C. Huntington, F. Fiuza, J. Ross, A. Zylstra, R. Drake, D. Froula, G. Gregori, N. Kugland, C. Kuranz, M. Levy, *et al.*, *Observation of magnetic field generation via the weibel instability in interpenetrating plasma flows*, Nature Physics **11**, 173–176 (2015).

[22]H.-S. Park, C. Huntington, F. Fiuza, R. Drake, D. Froula, G. Gregori, M. Koenig, N. Kugland, C. Kuranz, D. Lamb, *et al.*, *Collisionless shock experiments with lasers and observation of weibel instabilities*, Physics of Plasmas **22**, 056311 (2015).

[23]H.-S. Park, J. S. Ross, C. M. Huntington, F. Fiuza, D. Ryutov, D. Casey, R. P. Drake, G. Fiksel, D. Froula, G. Gregori, N. L. Kugland, C. Kuranz, M. C. Levy, C. K. Li, J. Meinecke, T. Morita, R. Petrasso, C. Plechaty, B. Remington, Y. Sakawa, A. Spitkovsky, H. Takabe, and A. B. Zylstra, *Laboratory astrophysical collisionless shock experiments on omega and NIF*, Journal of Physics: Conference Series **688**, 012084 (2016).

[24]J. Ross, D. Higginson, D. Ryutov, F. Fiuza, R. Hatarik, C. Huntington, D. Kalantar, A. Link, B. Pollock, B. Remington, *et al.*, *Transition from collisional to collisionless regimes in interpenetrating plasma flows on the national ignition facility*, Physical Review Letters **118**, 185003 (2017).

[25]C. Courtois, R. Grundy, A. Ash, D. Chambers, N. Woolsey, R. Dendy, and K. McClements, *Experiment on collisionless plasma interaction with applications to supernova remnant physics*, Physics of Plasmas **11**, 3386–3393 (2004).

[26]D. Yuan, H. Wei, G. Liang, F. Wang, Y. Li, Z. Zhang, B. Zhu, J. Zhao, W. Jiang, B. Han, *et al.*, *Laboratory study of astrophysical collisionless shock at sg-ii laser facility*, High Power Laser Science and Engineering **6** (2018).

[27]Y. Kuramitsu, Y. Sakawa, T. Morita, C. Gregory, J. Waugh, S. Dono, H. Aoki, H. Tanji, M. Koenig, N. Woolsey, *et al.*, *Time evolution of collisionless shock in counterstreaming laser-produced plasmas*, Physical Review Letters **106**, 175002 (2011).

[28]C. Li, V. Tikhonchuk, Q. Moreno, H. Sio, E. D'Humières, X. Ribeyre, P. Korneev, S. Atzeni, R. Betti, A. Birkel, *et al.*, *Collisionless shocks driven by supersonic plasma flows with self-generated magnetic fields*, Physical Review Letters **123**, 055002

(2019).
[29]G. Swadling, C. Bruulsema, F. Fiuza, D. Higginson, C. Huntington, H. Park, B. Pollock, W. Rozmus, H. Rinderknecht, J. Katz, *et al.*, *Measurement of kinetic-scale current filamentation dynamics and associated magnetic fields in interpenetrating plasmas*, Physical Review Letters **124**, 215001 (2020).
[30]F. Fiuza, G. Swadling, A. Grassi, H. Rinderknecht, D. Higginson, D. Ryutov, C. Bruulsema, R. Drake, S. Funk, S. Glenzer, *et al.*, *Electron acceleration in laboratory-produced turbulent collisionless shocks*, Nature Physics **16**, 916–920 (2020).
[31]D. Schaeffer, E. Everson, D. Winske, C. Constantin, A. Bondarenko, L. Morton, K. Flippo, D. Montgomery, S. Gaillard, and C. Niemann, *Generation of magnetized collisionless shocks by a novel, laser-driven magnetic piston*, Physics of Plasmas **19**, 070702 (2012).
[32]C. Niemann, W. Gekelman, C. Constantin, E. Everson, D. Schaeffer, A. Bondarenko, S. Clark, D. Winske, S. Vincena, B. Van Compernolle, *et al.*, *Observation of collisionless shocks in a large current-free laboratory plasma*, Geophysical Research Letters **41**, 7413–7418 (2014).
[33]D. Schaeffer, W. Fox, D. Haberberger, G. Fiksel, A. Bhattacharjee, D. Barnak, S. Hu, and K. Germaschewski, *Generation and evolution of high-mach-number laser-driven magnetized collisionless shocks in the laboratory*, Physical Review Letters **119**, 025001 (2017).
[34]D. B. Schaeffer, W. Fox, D. Haberberger, G. Fiksel, A. Bhattacharjee, D. Barnak, S. Hu, K. Germaschewski, and R. Follett, *High-mach number, laser-driven magnetized collisionless shocks*, Physics of Plasmas **24**, 122702 (2017).
[35]D. B. Schaeffer, W. Fox, R. Follett, G. Fiksel, C. Li, J. Matteucci, A. Bhattacharjee, and K. Germaschewski, *Direct observations of particle dynamics in magnetized collisionless shock precursors in laser-produced plasmas*, Physical Review Letters **122**, 245001 (2019).
[36]L. Romagnani, S. Bulanov, M. Borghesi, P. Audebert, J. Gauthier, K. Löwenbrück, A. Mackinnon, P. Patel, G. Pretzler, T. Toncian, *et al.*, *Observation of collisionless shocks in laser-plasma experiments*, Physical Review Letters **101**, 025004 (2008).
[37]A. Rigby, F. Cruz, B. Albertazzi, R. Bamford, A. R. Bell, J. E. Cross, F. Fraschetti, P. Graham, Y. Hara, P. M. Kozlowski, *et al.*, *Electron acceleration by wave turbulence in a magnetized plasma*, Nature Physics **14**, 475–479 (2018).
[38]H. Ahmed, M. E. Dieckmann, L. Romagnani, D. Doria, G. Sarri, M. Cerchez, E. Ianni, I. Kourakis, A. L. Giesecke, M. Notley, *et al.*, *Time-resolved characterization of the formation of a collisionless shock*, Physical Review Letters **110**, 205001 (2013).
[39]J. Jiao, S. He, H. Zhuo, B. Qiao, M. Yu, B. Zhang, Z. Deng, F. Lu, K. Zhou, X. Wang, *et al.*, *Experimental observation of ion–ion acoustic instability associated with collisionless shocks in laser-produced plasmas*, The Astrophysical Journal Letters **883**, L37 (2019).
[40]B. Albertazzi, J. Béard, A. Ciardi, T. Vinci, J. Albrecht, J. Billette, T. Burris-Mog, S. Chen, D. Da Silva, S. Dittrich, *et al.*, *Production of large volume, strongly magnetized laser-produced plasmas by use of pulsed external magnetic fields*, Review of Scientific Instruments **84**, 043505 (2013).
[41]W. Yao, B. Qiao, Z. Zhao, Z. Lei, H. Zhang, C. Zhou, S. Zhu, and X. He, *Kinetic particle-in-cell simulations of the transport of astrophysical relativistic jets in magnetized intergalactic medium*, The Astrophysical Journal **876**, 2 (2019).
[42]D. Schaeffer, W. Fox, J. Matteucci, K. Lezhnin, A. Bhattacharjee, and K. Germaschewski, *Kinetic simulations of piston-driven collisionless shock formation in magnetized laboratory plasmas*, Physics of Plasmas **27**, 042901 (2020).
[43]D. Higginson, P. Korneev, C. Ruyer, R. Riquier, Q. Moreno, J. Béard, S. Chen, A. Grassi, M. Grech, L. Gremillet, *et al.*, *Laboratory investigation of particle acceleration and magnetic field compression in collisionless colliding fast plasma flows*, Communications Physics **2**, 1–7 (2019).
[44]D. Higginson, G. Revet, B. Khiar, J. Béard, M. Blecher, M. Borghesi, K. Burdonov, S. Chen, E. Filippov, D. Khaghani, *et al.*, *Detailed characterization of laser-produced astrophysically-relevant jets formed via a poloidal magnetic nozzle*, High Energy Density Physics **23**, 48–59 (2017).
[45]B. Khiar, G. Revet, A. Ciardi, K. Burdonov, E. Filippov, J. Béard, M. Cerchez, S. Chen, T. Gangolf, S. Makarov, *et al.*, *Laser-produced magnetic-rayleigh-taylor unstable plasma slabs in a 20 t magnetic field*, Physical Review Letters **123**, 205001 (2019).
[46]E. Filippov, S. Makarov, K. Burdonov, W. Yao, G. Revet, J. Béard, S. Bolaños, S. Chen, A. Guediche, J. Hare, *et al.*, *Enhanced x-ray emission arising from laser-plasma confinement by a strong transverse magnetic field*, arXiv preprint arXiv:2006.12424 (2020).
[47]S. Giagkiozis, S. N. Walker, S. A. Pope, and G. Collinson, *Validation of single spacecraft methods for collisionless shock velocity estimation*, Journal of Geophysical Research: Space Physics **122**, 8632–8641 (2017).
[48]A. Y. Faenov, S. A. Pikuz, A. I. Erko, B. A. Bryunetkin, *et al.*, *High-performance X-ray Spectroscopic Devices for Plasma Microsources Investigations*, Phys. Scr. **50**, 333–338 (1994).
[49]S. N. Ryazantsev, I. Y. Skobelev, A. Y. Faenov, T. A. Pikuz, A. N. Grum-Grzhimailo, and S. A. Pikuz, *X-ray spectroscopy diagnostics of a recombining plasma in laboratory astrophysics studies*, JETP Letters **102**, 707–712 (2015).
[50]E. D. Filippov, I. Y. Skobelev, G. Revet, S. N. Chen, B. Khiar, A. Ciardi, D. Khaghani, D. P. Higginson, S. A. Pikuz, and J. Fuchs, *X-ray spectroscopy evidence for plasma shell formation in experiments modeling accretion columns in young stars*, Matter and Radiation at Extremes **4**, 064402 (2019).
[51]S. Wilks, W. Kruer, M. Tabak, and A. Langdon, *Absorption of ultra-intense laser pulses*, Physical review letters **69**, 1383 (1992).
[52]S. Bolanos, R. Smets, S. Chen, A. Grisolet, E. Filippov, J. Henares, V. Nastasa, S. Pikuz, R. Riquier, M. Safranova, *et al.*, *Laboratory evidence of the halting of magnetic reconnection by a weak guide field*, arXiv preprint arXiv:1909.01684 (2019).
[53]D. H. Froula, N. C. Luhmann Jr, J. Sheffield, and S. H. Glenzer, *Plasma scattering of electromagnetic radiation: theory and measurement techniques* (Elsevier, 2011).
[54]D. Froula, J. Ross, B. Pollock, P. Davis, A. James, L. Divol, M. Edwards, A. Offenberger, D. Price, R. Town, *et al.*, *Quenching of the nonlocal electron heat transport by large external magnetic fields in a laser-produced plasma measured with imaging thomson scattering*, Physical Review Letters **98**, 135001 (2007).
[55]A. Mančić, J. Fuchs, P. Antici, S. Gaillard, and P. Audebert, *Absolute calibration of photostimulable image plate detectors used as (0.5–20 mev) high-energy proton detectors*, Review of Scientific Instruments **79**, 073301 (2008).
[56]B. Fryxell, K. Olson, P. Ricker, F. Timmes, M. Zingale, D. Lamb, P. MacNeice, R. Rosner, J. Truran, and H. Tufo, *Flash: An adaptive mesh hydrodynamics code for modeling astrophysical thermonuclear flashes*, The Astrophysical Journal Supplement Series **131**, 273 (2000).
[57]A. Kemp and J. Meyer-ter Vehn, *An equation of state code for hot dense matter, based on the qeos description*, Nuclear Instruments and Methods in Physics Research Section A: Accelerators, Spectrometers, Detectors and Associated Equipment **415**, 674–676 (1998).
[58]M. Haines, *Magnetic-field generation in laser fusion and hot-electron transport*, Canadian Journal of Physics **64**, 912–919 (1986).
[59]C. K. Li, F. H. Séguin, J. A. Frenje, J. R. Rygg, R. D. Petrasso, R. P. J. Town, P. A. Amendt, S. P. Hatchett, O. L. Landen, A. J. Mackinnon, P. K. Patel, V. A. Smalyuk, T. C. Sangster, and J. P. Knauer, *Measuring e and b fields in laser-produced plasmas with monoenergetic proton radiography*, Phys. Rev. Lett. **97**, 135003 (2006).
[60]L. Gao, P. M. Nilson, I. V. Igumenshchev, M. G. Haines, D. H. Froula, R. Betti, and D. D. Meyerhofer, *Precision mapping of*

laser-driven magnetic fields and their evolution in high-energy-density plasmas, Physical Review Letters **114**, 215003 (2015).

[61] C. A. Cecchetti, M. Borghesi, J. Fuchs, G. Schurtz, S. Kar, A. Macchi, L. Romagnani, P. A. Wilson, P. Antici, R. Jung, J. Osterholtz, C. A. Pipahl, O. Willi, A. Schiavi, M. Notley, and D. Neely, *Magnetic field measurements in laser-produced plasmas via proton deflectometry*, Physics of Plasmas **16**, 043102 (2009).

[62] J. Derouillat, A. Beck, F. Pérez, T. Vinci, M. Chiaramello, A. Grassi, M. Flé, G. Bouchard, I. Plotnikov, N. Aunai, *et al.*, *Smilei: A collaborative, open-source, multi-purpose particle-in-cell code for plasma simulation*, Computer Physics Communications **222**, 351–373 (2018).

[63] S. Matsukiyo and M. Scholer, *Modified two-stream instability in the foot of high mach number quasi-perpendicular shocks*, Journal of Geophysical Research: Space Physics **108** (2003).

[64] L. Woods, *Shock Waves in Collisionless Plasmas*, edited by D. Tidman and N. Krall (Wiley, New York, 1971).

[65] D. Burgess and M. Scholer, *Shock front instability associated with reflected ions at the perpendicular shock*, Physics of Plasmas **14**, 012108 (2007).